Nano Research 2019, 12(6): 1423–1429

ISSN 1998-0124 CN 11-5974/O4
https://doi.org/10.1007/s12274-019-2376-x

Research Article

Wheat straw-derived magnetic carbon foams: *In-situ* preparation and tunable high-performance microwave absorption

Guangjun Gou, Fanbin Meng (✉), Huagao Wang, Man Jiang, Wei Wei, and Zuowan Zhou (✉)

Key Laboratory of Advanced Technologies of Materials (Ministry of Education), School of Materials Science and Engineering, Southwest Jiaotong University, Chengdu 610031, China

Received: 30 January 2019 / **Revised:** 6 March 2019 / **Accepted:** 9 March 2019

ABSTRACT

Recently, biomass-derived three-dimensional (3D) porous carbon materials have been gaining more interest as promising microwave absorbers due to their low cost, vast availability, and sustainability. Here, a novel 3D interconnected porous magnetic carbon foams are *in-situ* synthesized via a combination of sol-gel and carbonization process with wheat straw as the carbon source and $FeCl_3{\cdot}6H_2O$ as the magnetic regulating agent. During the process of foams formation, the lignocelluloses from the steam-exploded wheat straw are converted into interconnected carbon sheet networks with hierarchical porous structures, and the precursor $FeCl_3{\cdot}6H_2O$ is converted into magnetic nanoparticles uniformly embedded in the porous carbon foams. The generated magnetic nanoparticles are benefit to enhance the interface polarization and magnetic loss ability to improve the efficient complementarities between the dielectric and magnetic loss, thus increasing the impedance matching. The obtained sample treated at 600 °C displays the best microwave absorption (MA) performance. It presents a minimal reflection loss (RL) of −43.6 dB at 7.1 GHz and the effective bandwidth (RL < −10 dB) is 3.3 GHz with the thickness of 4.7 mm. The 3D porous structure, multi-interfaces and the synergy of dielectric loss and magnetic loss make great contribution to the outstanding MA performance.

KEYWORDS

wheat straw, magnetic biomass carbon foams, microwave absorption, interface polarization, impedance matching

1 Introduction

To solve the more and more serious electromagnetic wave interference issue, many efforts have been done to search for high-performance microwave absorption (MA) materials, which can effectively absorb the incident microwaves by transforming them into heat through magnetic/dielectric loss or dissipating them through interference [1–4]. Nevertheless, developing MA materials with special features of broad frequency, low density, strong absorption intensity, low thickness, and high thermal stability is still a challenge [5]. Among the MA materials, combination of dielectric lossy carbon materials (graphene, carbon nanotubes, helical carbon nanotubes, etc.) and magnetic lossy materials (magnetic metals, ferrites, and magnetic oxides) has gained more attention to broaden the effective bandwidth of MA materials, such as Fe_xO_y/rGO [6, 7], rGO/MoS_2 [8], N-rGO/$FeNi_3$ [9], CNTs/Fe_3O_4 [10], $CuFe_{10}Al_{12}O_{19}$/MWCNT [11], RGO/MWCNTs/$ZnFe_2O_4$ [12]. This combination strategy can not only improve the impedance matching but also enhance MA attenuation deriving from the efficient complementarities between the dielectric loss and magnetic loss [13]. Besides, design of absorbers structure with special morphologies is another important strategy to impact on the density and the microwave absorption performance. Among the various structures, porous/hollow structure has been anticipated to be one of the most promising candidates for MA applications, not only due to the high interfacial polarization and enhanced multiple scattering of incident microwaves, but also for their lightweight and low-density features, which are of great importance for the MA materials [14, 15]. Furthermore, porous structures are advantageous for incorporating different types of nanoparticles to obtain better MA materials due to improving impedance matching [16, 17]. As reported, porous carbon nanowires, fibers, nanotubes, graphene foams and their related composites have been synthesized and proved to get high-performance MA. Nevertheless, these kinds of materials display some disadvantages for MA application, such as toxic precursors, high costs, and complicated synthesis process, which noticeably hamper their commercialization. Therefore, it is still necessary to search low-cost porous carbonaceous materials with excellent MA properties.

Recently, to reduce the cost of the porous carbon materials, renewable precursors such as biomass or bio-wastes are highly expected to be explored to produce high-performance carbonaceous MA materials [18, 19]. Wheat straw, an important source of lignocellulose biomass of agricultural residue, is usually burned or used as animal feed and bedding materials [20]. Therefore, take full advantage of lignocellulose biomass from wheat straw as the carbonaceous MA materials seems to be an efficient strategy due to their low cost, abundance, and relatively high carbon content [21–23]. Furthermore, the use of lignocelluloses other than three primarily polymeric components in wheat straw (cellulose, hemicellulose, and lignin) is mainly due to the isolation of each components always involving in hazardous chemicals and environmental pollution [24]. To get high quality lignocellulose, hydroxide anion is considered as an ideal substitution reported by Zhong [25]. Furthermore, in order to increase the dissolution of lignocellulose, steam-exploded pretreatment is further applied [26]. Therefore, in this study the wheat straw was pretreated by steam explosion, and

---

Address correspondence to Fanbin Meng, mengfanbin_wing@126.com; Zuowan Zhou, zwzhou@swjtu.edu.cn

then mixed $FeCl_3·6H_2O$ with dissolving in tetrabutylammonium hydroxide (TBAH)/dimethyl sulfoxide (DMSO) aqueous solution to obtain Fe^{3+} chelated lignocellulose foams through sol-gel and freeze-drying. The magnetic lignocellulose-derived porous carbon foams were formed after carbonization. During the carbonization process, the Fe^{3+} salt was transferred into iron oxide nanoparticles embedded in the porous carbon, which are not only benefit to the impedance matching behavior for MA applications, but also increasing the interface polarization and magnetic loss ability.

2 Experimental

2.1 Raw materials

The wheat straws were collected from the suburb of Deyang City in Sichuan Province, China. A pre-treatment process must be carried out by steam explosion. The straws were heated with steam up to 2.6 MPa for 40 min, and then the exploded sample was oven-dried at 70 °C for 24 h. After that, the obtained samples were milled in order to pass through a 380 μm particle size sieve. $FeCl_3·6H_2O$ and DMSO were provided by Chengdu Kelong Chemical Reagent Co. Ltd. (Chengdu, China). The aqueous solution of TBAH (15 wt.%) was supplied by Runjing Chemical Co. Ltd. (Zhenjiang, China). All chemical regents used were of analytical and used without further purification.

2.2 Preparation of magnetic carbon foams

The fabrication process of the magnetic carbon foams is shown in Scheme 1. Firstly, the obtained dried steam-exploded wheat straws (0.6 g) were swelled in DMSO (16.3 g), and then the lignocellulose was dissolved by adding the aqueous solution containing TBAH 50% (3.1 g) with magnetic stirring for 1 h. After dissolution, the mixture was separated by centrifuging. $FeCl_3·6H_2O$ (1.0 g) was dissolved in the 2 mL DMSO under stirring to obtain yellow homogeneous solution. Subsequently, the yellow solution was mixed with the obtained lignocellulose solution and stirred to ensure homogeneity. The mixed gel solution was then poured into a cylindrical weighing bottle and then immediately immersed in water for 24 h. This immersion process was repeated several times until the formation of a cylindrical hydrogel. Finally, the gel underwent was freeze-dried to obtain the lignocellulose-based foams (Fig. S1 in the Electronic Supplementary Material (ESM)). After that, the obtained porous materials were transferred into a tubular furnace (OTF1200X, Hefei Kejing Materials Technology Co. Ltd., China) for pyrolysis. It was heated up to various temperatures (500–700 °C) for 2 h at 2 °C·min^{-1} under an argon atmosphere to get magnetic lignocellulose-based porous carbon. The samples annealed at different temperatures (500, 600, and 700 °C) are named MLPC-500, MLPC-600 and MLPC-700.

2.3 Characterization

X-ray diffraction (XRD) analysis was carried out on a Bruker D8 ADVANCE A25X XRD instrument with Cu Kα (target) radiation (λ = 1.5418 Å) at a scan rate (2θ) of 4 °·min^{-1} and a scan range from 5° to 80°. The bonding states of carbon were evaluated by a Thermo fisher in Via DXR Raman microscopes using 532 nm incident radiations. X-ray photoelectron spectroscopy (XPS) was measured using Thermo fisher Escalab 250Xi spectrometer. The morphologies were characterized on a field emission scanning electron microscopy (FE-SEM, JEOL, JSM-7001F) and a transmission electron microscopy (TEM, JEOL, JEM-2100F). The pore structures of the samples were measured by N_2 adsorption–desorption isotherms on a physisorption analyzer (JWGB, JW-BK132F) at 77 K for P/P_0 of 0.01–0.99. The complex permeability and permittivity were measured in the frequency of 2–18 GHz with a vector network analyzer (AV3618, CETC, China). Before testing, the samples mixed with wax at a mass ratio of 30 wt.% were pressed into toroidal rings (7.0 mm in outer diameter, 3.0 mm in inner diameter, and 3.0 mm in thickness). Finally, the reflection losses (RL) values of the composites were calculated based on the transmission line theory, using the measured values of complex permeability and permittivity.

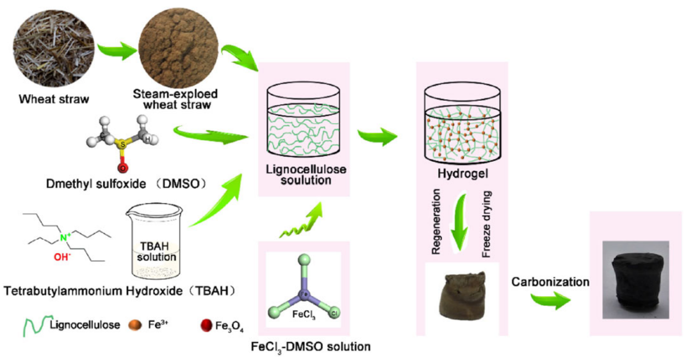

Scheme 1 Schematic of the fabrication of the magnetic carbon foams.

3 Results and discussion

XRD is first used to analyze the crystalline structure of the as-prepared magnetic carbon foams (Fig. 1(a)). The diffraction peaks 30.1°, 35.5°, 43.1°, 53.6°, 57.1°, and 62.3° can be assigned to the (220), (311), (400), (422), (511), and (440) of crystal planes of the face-centered cubic lattice of Fe_3O_4 (JCPDS card No. 01-1111, marked as "♣"). Besides, two additional diffraction peaks at 44.7° and 65.2° can be found in MLPC-600 and MLPC-700, which are attributed to the (110) and (200) crystal planes of α-Fe (JSPDF Card No: 06-0696, marked as "◆") due to the partial reduction of Fe_3O_4 after further carbonization treatment. Interestingly, the diffraction peaks intensity of Fe become stronger with the increase of carbonization temperature, indicating the growing content of Fe [27]. Therefore, more interfaces between Fe_3O_4 and Fe could be generated, which is in favor of interface polarization, thus enhancing the MA performance. In addition, there are no obvious diffraction peaks at about 24° and 43° of carbon materials. This is because the carbonized biomass-based carbon is existence of low graphitization degree of carbon [2]. Raman spectra are used to investigate the structures of carbonaceous

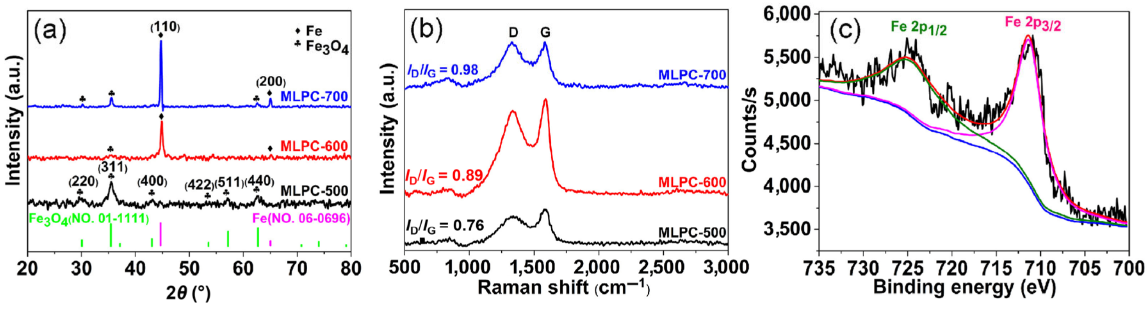

Figure 1 (a) XRD patterns of MLPC composites. (b) The Raman spectra of all the samples. (c) XPS spectrum of Fe 2p of sample MLPC-600.

materials. As displayed in Fig. 1(b), the D band at about 1,330 cm^{-1} is induced by disorder carbon or defective graphite and the G band at about 1,590 cm^{-1} corresponds to the graphitic layer [28]. The intensity ratio of D band to G band (I_D/I_G) is generally utilized to determine the defects within the carbon materials [29]. The I_D/I_G ratios of composites with various carbon temperatures (500, 600, and 700 °C) are 0.76, 0.89, 0.98, respectively, indicating that defect is increasingly generated with elevating annealing temperature, probably associated to more armchair edges of graphite [30]. The existing of amorphous carbon leads to defects, which might act as effective polarization centers when exposed to electromagnetic wave irradiation, contributing to the MA performance [31]. In order to further analyze the composition of the as-obtained foams, the component analysis is conducted by XPS. Three elements (C, O, Fe) can be found in all samples (Fig. S2 in the ESM). Further, the high-resolution Fe 2p XPS spectrum of MLPC-600 is used to distinguish the difference between Fe^{2+} and Fe^{3+} (Fig. 1(c)). The characteristic peaks of Fe_3O_4 were observed at 711.2 and 725.2 eV (Fig. 1(c)), corresponding to the Fe 2p$_{3/2}$ and Fe 2p$_{1/2}$, respectively [32]. Especially, no satellite peak at about 719.0 eV of α-Fe_2O_3, γ-Fe_2O_3 can be observed, further indicating that the information of the mixed Fe^{2+} and Fe^{3+} oxide is Fe_3O_4. However, peak located around 707 eV corresponding to α-Fe phase is not observed, suggesting that the Fe may be covered by the carbon in MLPC-600. Thus, all those results suggest that Fe_3O_4 is successfully prepared in the composite.

The morphologies of the obtained samples are further studied by SEM, as shown in Figs. 2(a)–2(d). Before carbonization, the pure lignocellulose foams exhibit a typical crosslinked three-dimensional (3D) network structure with two-dimensional (2D) sheet-like skeleton (Fig. 2(a)) (the pore size ranging from 2 to 3 μm), which seems to be caused by ice crystal formation during the freezing process due to the trapped water in the lignocellulose hydrogel, leading to squeezing out of lignocellulose to form the film-like structure [33, 34]. When Fe^{3+} is introduced, many pores are generated in the 2D sheet-like skeleton, and the pore size of 3D network increases to 2–4 μm compared to that without Fe^{3+} (Fig. 2(b)), which may be attributed to the cross-linking reaction between Fe^{3+} and abundant functional groups (such as –COOH, –OH) of lignocellulose [35, 36]. After carbonization at 600 °C, the 3D network structure still exists, but its pore size of 3D network reduces due to the carbonization reaction [2]. Furthermore, the generated Fe_3O_4 nanoparticles can't be clearly observed due to extremely small size, which can be characterized by the following TEM images. However, the corresponding element mappings of C, O, and Fe can confirm the uniform distribution of Fe_3O_4 nanoparticles within the interconnected networks (Fig. 2(d)). Besides, the carbonization temperature also influences the pore size of 3D network, and its size will be reduced with the increase of carbonization temperature by comparing MLPC-500, MLPC-600 and MLPC-700 (Fig. 2(c) and Fig. S3 in the ESM). TEM and high-resolution TEM (HRTEM) are carried out to further investigate the microstructures of as-obtained MLPC-600. As shown in Fig. 2(e), there exists obvious 3D cross-linked porous network structure, and numerous of ultra-small Fe_3O_4 nanoparticles with average size of 9 nm also can be observed and embed in carbon sheets without aggregation. Meanwhile, the HRTEM image (Fig. 2(f)) further presents the lattice fringes with *d*-spacing values of 0.25 nm, corresponding to the (311) plane of Fe_3O_4 [37]. This is consistent with the XRD analysis (Fig. 1(a)). Moreover, as the increase of carbonization temperature, the size of Fe_3O_4 nanoparticles gradually increases accompanied by serious agglomeration (Fig. S4 in the ESM).

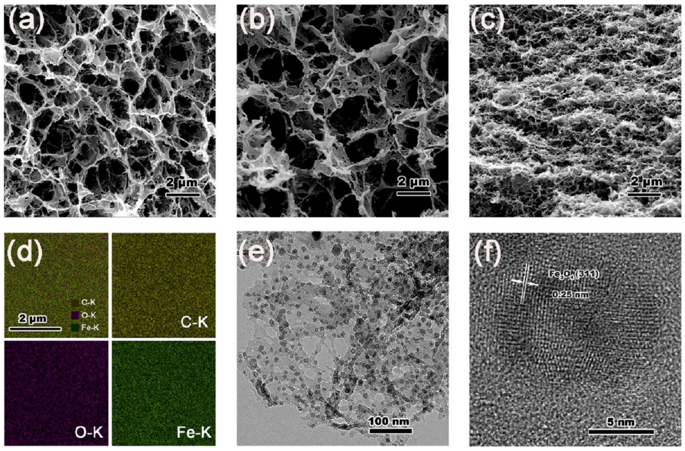

Figure 2 SEM images of the lignocellulose foams without Fe^{3+} (a) and with Fe^{3+} (b), magnetic carbon foams under carbonization temperature 600 °C: MLPC-600 (c), with corresponding elemental mapping (d), TEM image of MLPC-600 (e) and HRTEM image of MLPC-600 (f).

The porous structures of the products are further measured by nitrogen adsorption–desorption isotherms (Fig. 3). Figure 3(a) shows that all three samples exhibit a typical type H3 hysteresis loop according to the International Union of Pure and Applied Chemistry (IUPAC), indicating the existence of mesoporous structure in MLPC. Figure 3(b) displays the pore size distribution curves of MLPC-500, MLPC-600, and MLPC-700 calculated by the Barret–Joyner–Halender (BJH) method using the desorption isotherms. It can be seen that all three samples show dominant pore size regions in the range of 2.0–7.0 nm. The Brunauer–Emmett–Teller (BET) surface areas, average pore sizes and pore volumes of MLPC-500, MLPC-600, and MLPC-700 are summarized in Table 1. Among them, MLPC-600 demonstrated an ultrahigh BET surface area of 293 m^2·g^{-1} with very good pore volume of 0.30 cm^3·g^{-1} and pore size of 4.55 nm. As discussed above, the porous structure not only provides the composites with large specific surface area and total pore volume but also produces multiple reflections and scattering for energy dissipation, converting microwave energy to heat or other energy during prolonged propagation. Moreover, the porous structure contributes to reducing the weight density of the absorber.

Based on the structure characters, we study the electromagnetic properties of composites. Electromagnetic absorber has the ability to convert the electromagnetic wave into thermal energy due to their intrinsic physical features [38–40]. According to the electromagnetic energy conversion theory, the real permittivity (ε') and the real permeability (μ') represent the ability to store electric and magnetic energy, while the imaginary permittivity (ε'') and the

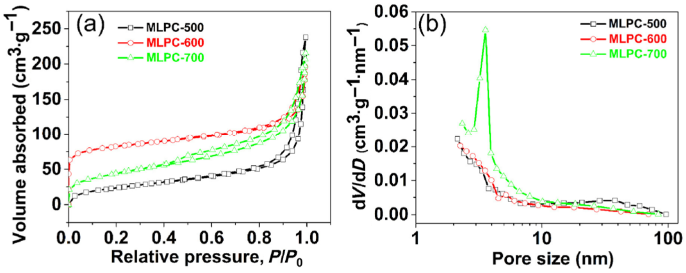

Figure 3 (a) N_2 absorption–desorption isotherms and (b) the pore size distributions calculated using BJH method of MLPC-500, MLPC-600 and MLPC-700.

Table 1 Pore properties of the products

Sample	S_{BET}^a (m^2·g^{-1})	V_{total}^b (cm^3·g^{-1})	D_p^d (nm)
MLPC-500	82	0.37	16.3
MLPC-600	293	0.30	4.55
MLPC-700	152	0.33	8.54

[a] Specific surface area estimated using BET method.

[b] Total pore volume calculated using single-point method at $P/P_0 = 0.99$.

[c] Pore size calculated using BJH method.

imaginary permeability (μ'') represent the dissipation of dielectric and magnetic energy [41, 42].

To obtain the complex relative permittivity and permeability, two equations are used [43]

$$\varepsilon_{\gamma} = \varepsilon' - j\varepsilon'' \quad \text{and} \quad \mu_{\gamma} = \mu' - j\mu'' \tag{1}$$

The complex permittivity plots of MLPC carbonized at various temperatures are shown in Figs. 4(a) and 4(b). It can be found that ε' and ε'' values of samples decrease roughly with the increasing of treatment temperature. The ε' and ε'' values of MLPC-500 keep nearly stable in the frequency of 2–18 GHz. The ε' and ε'' values of MLPC-600 roughly decrease with the increasing in the frequency of 2–4 GHz and keep nearly stable in the frequency of 4–18 GHz. The ε' and ε'' values of MLPC-700 decrease with the increasing in the frequency of 2–6 GHz and keep nearly stable in the frequency of 4–18 GHz. Four types of polarization occurs at a heterogeneous system, which can be called as electronic, atomic, Debye (dipolar) and interfacial polarization [44]. Generally, electronic, atomic polarizations exist at higher frequency [44], which can be excluded from the following discussion. According to Debye theory, the relationship of ε' and ε'' can be presented as [45]

$$\left(\varepsilon' - \frac{\varepsilon_s + \varepsilon_\infty}{2}\right)^2 + \left(\varepsilon''\right)^2 = \left(\frac{\varepsilon_s - \varepsilon_\infty}{2}\right)^2 \tag{2}$$

where ε_s indicates the static permittivity and ε_∞ presents the relative dielectric constant at the high-frequency limit. From Eq. (2), it can be concluded that the curves of ε' to ε'' for an absorber should be a semicircle during the Debye relaxation process. The semicircle is usually termed as the Cole–Cole semicircle, and each semicircle corresponds to a Debye relaxation process. Each Cole–Cole semicircle represents one Debye relaxation process. Figure S5 in the ESM shows the ε' vs. ε'' curves of MLPC-600 in the frequency of 2–18 GHz.

The Cole–Cole plots of MLPC-500 show an obvious semicircle (Fig. S5(a) in the ESM), indicating that the relaxation occurs due to interfacial polarization. The interfacial polarization results from the multiple interfaces including C/air, C/Fe_3O_4@Fe, Fe_3O_4@Fe. It is worth pointing out that the conductivity loss due to the enhanced conductive network in the foams should not be neglected even when no obvious semicircles in the high frequency region are observed. As the increase of carbonization temperature, the role of interface polarization is weakened. Meanwhile, the conduction loss plays a major contribution to dielectric loss, as show in Figs. S5(b) and S5(c) in the ESM.

Not only the relative complex permittivity but also the relative complex permeability can influence microwave absorption properties. μ' and μ'' of all composites with the carbonization treatment at 500–700 °C are given in Figs. 4(d) and 4(e). The μ' and μ'' values of samples increase with increasing temperature, it means that when the temperature is higher, as-prepared samples exhibit the good dissipation capability of magnetic energy, which is beneficial to microwave absorption.

In order to explain the mechanism of MA, we also calculated the dielectric loss tangent ($\tan\delta_E = \varepsilon''/\varepsilon'$) and the magnetic loss tangent ($\tan\delta_M = \mu''/\mu'$), as shown in Figs. 4(c) and 4(f). The composites treated at 500 °C show relative low dielectric loss factor among the range of whole frequency because of its small ε'' values, indicating poor dielectric loss. With the increasing of treatment temperature, the dielectric loss factor was improved. Correspondingly, the magnetic loss factor also enhances as the pyrolysis temperature rises. The MLPC-500 and MLPC-600 have close value of $\tan\delta_E$ and $\tan\delta_M$. But the difference between $\tan\delta_E$ and $\tan\delta_M$ of 700 °C is great. Therefore, treatment at 500 and 600 °C should have better impedance matching.

The magnetic loss is another vital factor that leads to electromagnetic wave attenuation in the composites. Generally, magnetic loss comes from the eddy current effects, exchange resonance and natural resonance in the microwave frequency band [46]. The resonance peaks of the μ'' at 2–8 GHz should correspond to natural resonance [47]. If the eddy current occurs on the composites, the C_o ($C_o = \mu''(\mu')^{-2}f^{-1}$) will be a constant [48]. Whereas, it can be seen in Fig. S6 in the ESM that the values of C_o are not fixed at the whole frequency region for the MLPC samples under various temperatures because the natural resonance might derive from the geometrical configuration effect. However, the C_o values of MLPC-500, MLPC-600, and MLPC-700 keep relatively constant in 13.6–15.8, 13.0–14.8, and 9.6–10.5 GHz, respectively, indicating that the magnetic loss partly comes from the eddy current loss. Also, according to Aharoni's theory which has been proved in ferromagnetic nanoparticles, the resonance at higher frequency should be caused by the exchange resonance [46].

Based on the above-mentioned electromagnetic wave parameters at a given absorber thickness and frequency, the refection loss (RL)

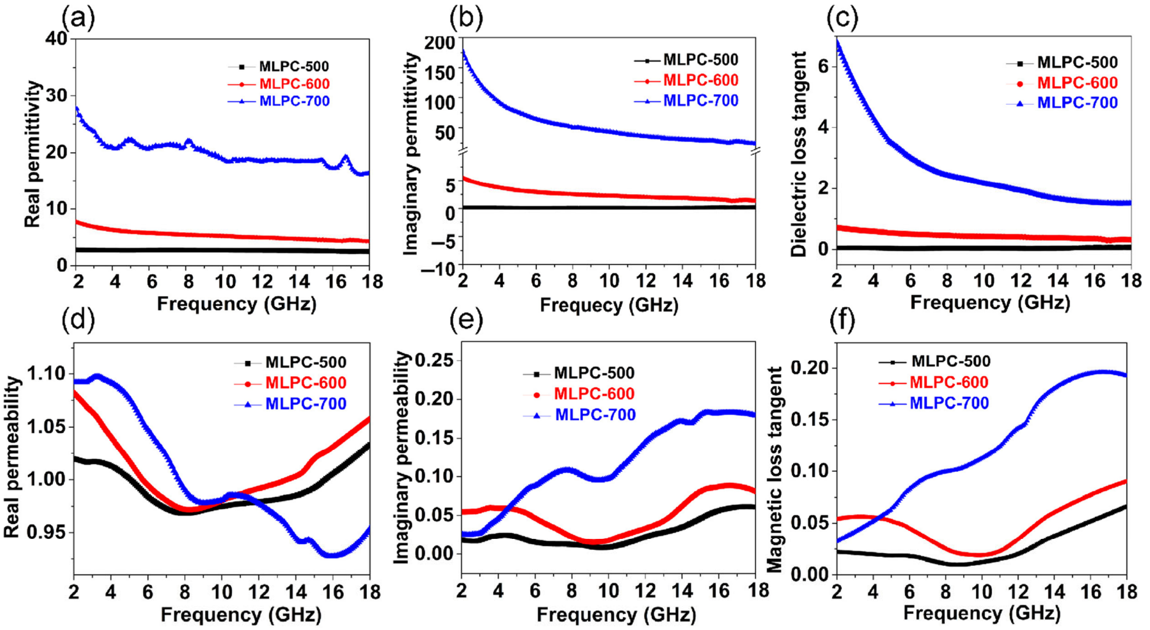

Figure 4 Frequency dependence of (a) the real part (ε') and (b) imaginary part (ε'') of complex permittivity, (c) dielectric loss ($\tan\delta_E$), (d) real part (μ') and (e) imaginary part (μ'') of complex permeability, and (f) magnetic loss ($\tan\delta_M$) for MLPC composites with various carbonization treatment in the 2–18 GHz.

value is used to evaluate the microwave absorption efficiency of materials and can be calculated by the following equations according to transmission line theory [49].

$$\mathrm{RL}\,(\mathrm{dB}) = 20\log\left|\frac{Z_{\mathrm{in}}-1}{Z_{\mathrm{in}}+1}\right| \tag{3}$$

$$Z_{\mathrm{in}} = Z_0\sqrt{\frac{\mu_\gamma}{\varepsilon_\gamma}}\tanh\left[\mathrm{j}\left(\frac{2\pi fd}{c}\right)\sqrt{\mu_\gamma\varepsilon_\gamma}\right] \tag{4}$$

where Z_{in} is the input impedance of the absorber, μ_{r} and ε_{r} are respectively the relative complex permeability and permittivity, f is the frequency of microwave, d is the thickness of the absorber, and c is the velocity of light in free space. Typically, the RL value is used to evaluate the microwave absorption efficiency of materials. When the value of reflection loss is below −10 dB, indicating that 90% of the electromagnetic energy will be absorbed. The RL values for the samples treatment at 500 and 700 °C (Figs. 5(a) and 5(c)) cannot reach −10 dB within the thickness range of 2.0–5.0 mm, indicating that the samples could not be used for practical applications. For the composite treatment at 600 °C (Fig. 5(b)), the RL values exceeding −10 dB, reached in the 6.0–17.5 GHz range with absorber thicknesses of 2.0–5.0 mm and a minimum RL of −43.6 dB is obtained at 7.1 GHz with the matching thickness of 4.7 mm. The results suggest that the composites have remarkable absorbing characteristics in wide frequency bands from the C to Ku band (4–18 GHz). Figure 5(d) shows the comparison of the minimum RL values at different matching thicknesses for the samples. The composite with 600 °C treatment exhibits remarkable microwave absorption properties at thickness of 4.7 mm when compared to the other two samples. The results demonstrate that the calcination temperature has a significant effect on the microwave absorption properties. Table S1 in the ESM summarizes the reflection loss performance of several excellent porous microwave absorption materials reported recently. Compared with other literatures, MLPC-600 has stronger absorption intensity (−43.6 dB), broader frequency bandwidth (11.5 GHz) and lightweight feature.

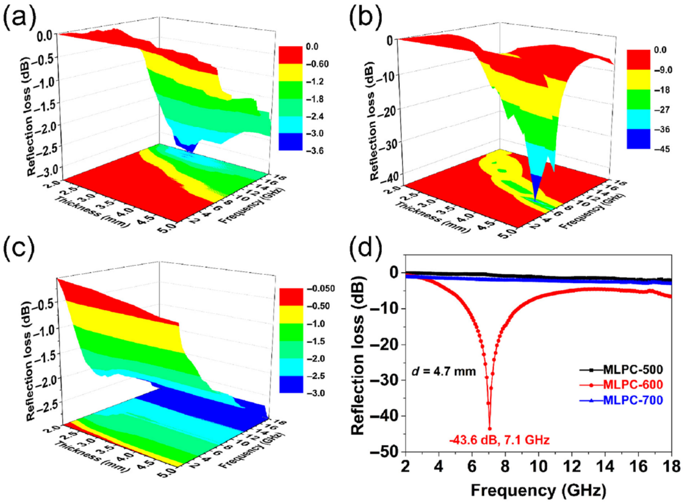

Figure 5 The three-dimensional representations wave reflection losses of the MPC materials ((a) MLPC-500, (b) MLPC-600, and (c) MLPC-700). (d) The comparison of minimum reflection loss of samples under the different temperatures.

In generally, the excellent electromagnetic wave absorption of MLPC-600 should be derived from the synergistic effects between the magnetic Fe_3O_4 and the dielectric amorphous carbons components, which result in the good impedance matching and strong electromagnetic wave attenuation in the interior of the absorber. The characteristic impedance of microwave-absorbing materials should be equal/close to that of free space (377 Ω), achieving zero reflection at the front surface of the materials. Thus, a delta-function method for validating impedance matching degree had been proposed in the following equation [50]

$$|\Delta| = \left|\sinh^2(Kfd) - M\right| \tag{5}$$

where K and M are further calculated by the complex permittivity and permeability through the presented below equations

$$K = \frac{4\pi\sqrt{\mu'\varepsilon'}\sin\dfrac{\delta_{\mathrm{e}}+\delta_{\mathrm{m}}}{2}}{c\cos\delta_{\mathrm{e}}\cos\delta_{\mathrm{m}}} \tag{6}$$

$$M = \frac{4\mu'\cos\delta_{\mathrm{e}}\cos\delta_{\mathrm{m}}}{(\mu'\cos\delta_{\mathrm{e}} - \varepsilon'\cos\delta_{\mathrm{m}})^2 + \left[\tan\left(\dfrac{\delta_{\mathrm{m}}-\delta_{\mathrm{e}}}{2}\right)\right]^2(\mu'\cos\delta + \varepsilon'\cos\delta)^2} \tag{7}$$

The small delta value and the area close to zero ($|\Delta| < 0.4$) usually mean good impedance matching. Figure 6 shows the calculated delta value maps of samples treatment at different temperature with thickness from 2 to 5 mm and frequency range from 2 to 18 GHz. Clearly, MLPC-500 (Fig. 6(a)) and MLPC-600 (Fig. 6(b)) have larger area close to zero as compared with MLPC-700 (Fig. 6(c)), suggesting that their employ excellent impedance match, which is corresponding to their superior microwave absorption performance. However, it is clear that the area close to zero of the sample treatment at 700 °C displays almost nonexistent (Fig. 6(c)), showing the quite high complex permittivity pushes them into the region of impedance mismatch. Based on the results, the porous sample treatment at 500 and 600 °C can not only carry out high perform special dielectric loss ability, but also be beneficial to improving the impedance matching, and these preferable advantages will lead to significantly enhancing microwave absorption properties.

As one of the most important factors in judging the high-efficiency MA property, the attenuation constant α is used to reflect the integral dissipation properties of materials, which can be calculated by the following equation [51]

$$\alpha = \frac{\sqrt{2}}{c}\pi f\sqrt{(\varepsilon''\mu'' - \varepsilon'\mu') + \sqrt{(\varepsilon''\mu'' - \varepsilon'\mu')^2 + (\varepsilon''\mu' + \varepsilon'\mu'')^2}} \tag{8}$$

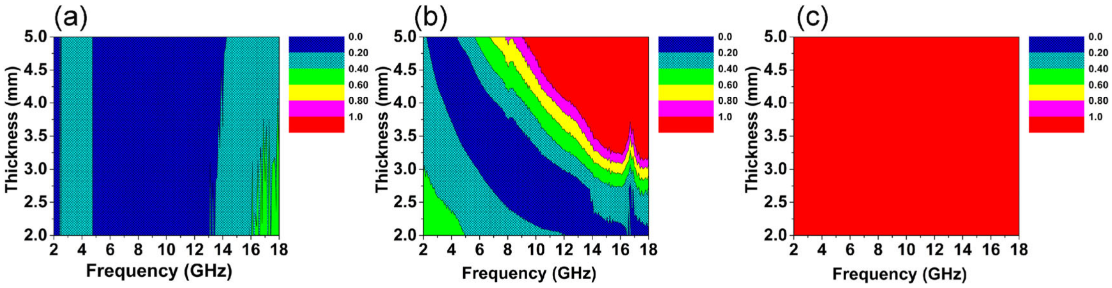

Figure 6 The calculated delta value maps of samples (a) MLPC-500, (b) MLPC-600 and (c) MLPC-700.

where f and c are the frequency and velocity of light, respectively. As shown in Fig. 7, MLPC-700 displayed the largest value over the whole frequency range. Though the attenuation constant of MLPC-600 is not the largest, the impedance matching is the best among them (Fig. 6(b)). Therefore, a relative balance between impedance matching and the attenuation factors is achieved and endows MLPC-600 with the best MA performance.

Overall, the enhanced MA performance of MLPC-600 should derive from the synergistic effects between straw-derived carbon foams and Fe_3O_4@Fe nanoparticles, which lead to the good impedance matching and multiple reflections and strong scatterings in the interior of the absorber. A schematic to clarify the potential absorbing mechanisms is proposed as shown in Fig. 8. According to Eq. (5) and corresponding calculated delta values (Fig. 6), MLPC-600 shows the optimal impedance matching, which implies the incident electromagnetic wave can enter this absorber with minimum reflection. After entering the absorber, the electromagnetic energy is then converted to heat energy by strong dielectric loss caused mostly by the conductive loss and partly by the interface polarization, and by the magnetic loss from natural resonance and exchange resonance of Fe_3O_4@Fe nanoparticles. Additionally, porous structures are beneficial for multiple reflections and scattering of microwave, which can increase the propagation paths for electromagnetic wave. Hence, the best impedance matching together with large attenuation capability endows MLPC-600 with the best MA performance.

4 Conclusions

In summary, a facile approach has been developed to prepare magnetic porous carbon materials with agricultural straw as the raw material and $FeCl_3\cdot 6H_2O$ as the regulating agent. The structure of the porous carbon can be adjusted by the annealing condition, resulting in an important effect on the MA properties. As an optimized result, the porous carbon treated at 600 °C exhibits excellent microwave absorption property due to the distinct 3D porous carbon framework and better impedance matching. The minimal reflection loss is −43.6 dB at 7.1 GHz and the effective bandwidth with 3.3 GHz when the thickness is 4.7 mm. Thus, we believe the approach presented in this work offers a new opportunity for microwave absorption from the renewable agricultural straws.

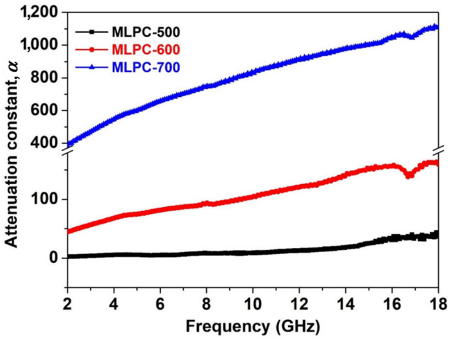

Figure 7 The values of attenuation constant (α) for composites in the frequency range of 2.0–18.0 GHz.

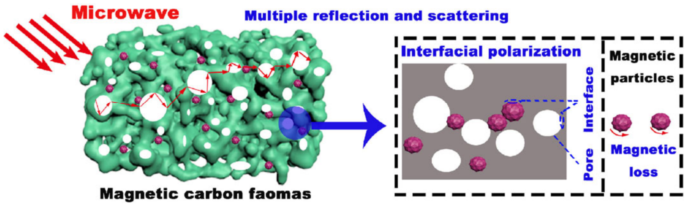

Figure 8 Schematic illustration of possible microwave absorption mechanisms of the MLPC absorbers.

Acknowledgements

This work was financially supported by the National Natural Science Foundation of China (No. 51573149), the Fundamental Research Funds for the Central Universities (No. 2682016CX069), the Science and Technology Planning Project of Sichuan Province (Nos. 2018GZ0132 and 2018GZ0427), and Sichuan Province Science and Technology Innovation Talent Project (No. 2017072).

Electronic Supplementary Material: Supplementary material (the photograph of Fe^{3+} chelated lignocellulose-based foams, XPS survey spectra of the composites, SEM and TEM images of MLPC-500 and MLPC-700, Core–Core plots for the composites, C_o–f curves of the three products and MA properties of porous carbon materials reported in recent literatures) is available in the online version of this article at https://doi.org/10.1007/s12274-019-2376-x.

References

[1] Sun, G. B.; Wu, H.; Liao, Q. L.; Zhang, Y. Enhanced microwave absorption performance of highly dispersed CoNi nanostructures arrayed on graphene. *Nano Res*. **2018**, *11*, 2689–2704.

[2] Wang, H. G.; Meng, F. B.; Li, J. Y.; Li, T.; Chen, Z. J.; Luo, H. B.; Zhou, Z. W. Carbonized design of hierarchical porous carbon/Fe_3O_4@Fe derived from loofah sponge to achieve tunable high-performance microwave absorption. *ACS Sustainable Chem. Eng*. **2018**, *6*, 11801–11810.

[3] Meng, F. B.; Wang, H. G.; Wei, W.; Chen, Z. J.; Li, T.; Li, C. Y.; Xuan, Y.; Zhou, Z. W. Generation of graphene-based aerogel microspheres for broadband and tunable high-performance microwave absorption by electrospinning-freeze drying process. *Nano Res*. **2018**, *11*, 2847–2861.

[4] Ding, Y.; Zhang, Z.; Luo, B. H.; Liao, Q. L.; Liu, S.; Liu, Y. C.; Zhang, Y. Investigation on the broadband electromagnetic wave absorption properties and mechanism of Co_3O_4-nanosheets/reduced-graphene-oxide composite. *Nano Res*. **2017**, *10*, 980–990.

[5] Liu, B.; Li, J. H.; Wang, L. F.; Ren, J. H.; Xu, Y. F. Ultralight graphene aerogel enhanced with transformed micro-structure led by polypyrrole nano-rods and its improved microwave absorption properties. *Compos. Part A: Appl. Sci. Manuf.* **2017**, *97*, 141–150.

[6] Meng, F. B.; Wang, H. G.; Huang, F.; Guo, Y. F.; Wang, Z. Y.; Hui, D.; Zhou, Z. W. Graphene-based microwave absorbing composites: A review and prospective. *Compos. Part B: Eng*. **2018**, *137*, 260–277.

[7] Zhou, N.; An, Q. D.; Xiao, Z. Y.; Zhai, S. R.; Shi, Z. Solvothermal synthesis of three-dimensional, Fe_2O_3 NPs-embedded CNT/N-doped graphene composites with excellent microwave absorption performance. *RSC Adv*. **2017**, *7*, 45156–45169.

[8] Zhang, D. Q.; Jia, Y. X.; Cheng, J. Y.; Chen, S. M.; Chai, J. X.; Yang, X. Y.; Wu, Z. Y.; Wang, H.; Zhang, W. J.; Zhao, Z. L. et al. High-performance microwave absorption materials based on MoS_2-graphene isomorphic hetero-structures. *J. Alloys Compd*. **2018**, *758*, 62–71.

[9] Feng, J.; Zong, Y.; Sun, Y.; Zhang, Y.; Yang, X.; Long, G. K.; Wang, Y.; Li, X. H.; Zheng, X. L. Optimization of porous $FeNi_3$/N-GN composites with superior microwave absorption performance. *Chem. Eng. J*. **2018**, *345*, 441–451.

[10] Li, N.; Huang, G. W.; Li, Y. Q.; Xiao, H. M.; Feng, Q. P.; Hu, N.; Fu, S. Y. Enhanced microwave absorption performance of coated carbon nanotubes by optimizing the Fe_3O_4 nanocoating structure. *ACS Appl. Mater. Interfaces* **2017**, *9*, 2973–2983.

[11] Bhattacharya, P.; Das, C. K. *In situ* synthesis and characterization of $CuFe_{10}Al_2O_{19}$/MWCNT nanocomposites for supercapacitor and microwave-absorbing applications. *Ind. Eng. Chem. Res*. **2013**, *52*, 9594–9606.

[12] Shu, R. W.; Li, W. J.; Zhou, X.; Tian, D. D.; Zhang, G. Y.; Gan, Y.; Shi, J. J.; He, J. Facile preparation and microwave absorption properties of RGO/MWCNTs/$ZnFe_2O_4$ hybrid nanocomposites. *J. Alloys Compd*. **2018**, *743*, 163–174.

[13] Han, M. K.; Yin, X. W.; Hou, Z. X.; Song, C. Q.; Li, X. L.; Zhang, L. T.; Cheng, L. F. Flexible and thermostable graphene/SiC nanowire foam composites with tunable electromagnetic wave absorption properties. *ACS Appl. Mater. Interfaces* **2017**, *9*, 11803–11810.

[14] Yang, Z. H.; Li, Z. W.; Yang, Y. H.; Xu, Z. C. J. Optimization of $Zn_xFe_{3-x}O_4$ hollow spheres for enhanced microwave attenuation. *ACS Appl.*

Mater. Interfaces **2014**, *6*, 21911–21915.

[15] Li, Y. N.; Wu, T.; Jiang, K. D.; Tong, G. X.; Jin, K. Y.; Qian, N. X.; Zhao, L. H.; Lv, T. X. Mn^{2+} induced structure evolution and dual-frequency microwave absorption of $Mn_xFe_{3-x}O_4$ hollow/porous spherical chains made by a one-pot solvothermal approach. *J. Mater. Chem. C* **2016**, *4*, 7119–7129.

[16] Liu, W.; Pan, J. J.; Ji, G. B.; Liang, X. H.; Cheng, Y.; Quan, B.; Du, Y. W. Switching the electromagnetic properties of multicomponent porous carbon materials derived from bimetallic metal-organic frameworks: Effect of composition. *Dalton Trans*. **2017**, *46*, 3700–3709.

[17] Zhang, H.; Hong, M.; Chen, P.; Xie, A. J.; Shen, Y. H. 3D and ternary rGO/MCNTs/Fe_3O_4 composite hydrogels: Synthesis, characterization and their electromagnetic wave absorption properties. *J. Alloy. Compd*. **2016**, *665*, 381–387.

[18] Deng, J.; Li, M. M.; Wang, Y. Biomass-derived carbon: Synthesis and applications in energy storage and conversion. *Green Chem*. **2016**, *18*, 4824–4854.

[19] Jin, H.; Wang, X. M.; Gu, Z. R.; Fan, Q. H.; Luo, B. A facile method for preparing nitrogen-doped graphene and its application in supercapacitors. *J. Power Sources* **2015**, *273*, 1156–1162.

[20] Perumal, A. B.; Sellamuthu, P. S.; Nambiar, R. B; Sadiku, E. R. Development of polyvinyl alcohol/chitosan bio-nanocomposite films reinforced with cellulose nanocrystals isolated from rice straw. *Appl. Surf. Sci*. **2018**, *449*, 591–602.

[21] Zhou, X.; Zhou, X. L.; Tang, X. S.; Xu, Y. Process for calcium xylonate production as a concrete admixture derived from *in-situ* fermentation of wheat straw pre-hydrolysate. *Bioresour. Technol*. **2018**, *261*, 288–293.

[22] Littlewood, J.; Murphy, R. J.; Wang, L. Importance of policy support and feedstock prices on economic feasibility of bioethanol production from wheat straw in the UK. *Renew. Sust. Energy Rev*. **2013**, *17*, 291–300.

[23] Wang, L.; Littlewood, J.; Murphy, R. J. Environmental sustainability of bioethanol production from wheat straw in the UK. *Renew. Sust. Energy Rev*. **2013**, *28*, 715–725.

[24] Chen, M. J.; Zhang, X. Q.; Zhang, A. P.; Liu, C. F.; Sun, R. C. Direct preparation of green and renewable aerogel materials from crude bagasse. *Cellulose* **2016**, *23*, 1325–1334.

[25] Zhong, C.; Wang, C. M.; Huang, F.; Jia, H. H.; Wei, P. Wheat straw cellulose dissolution and isolation by tetra-n-butylammonium hydroxide. *Carbohydr. Polym*. **2013**, 94, 38–45.

[26] Jiang, M.; Zhao, M. M.; Zhou, Z. W.; Huang, T.; Chen, X. L.; Wang, Y. Isolation of cellulose with ionic liquid from steam exploded rice straw. *Ind. Crops Prod*. **2011**, *33*, 734–738.

[27] Wu, G. L.; Cheng, Y. H.; Yang, Z. H.; Jia, Z. R.; Wu, H. J.; Yang, L. J.; Li, H. L.; Guo, P. Z.; Lv, H. L. Design of carbon sphere/magnetic quantum dots with tunable phase compositions and boost dielectric loss behavior. *Chem. Eng. J*. **2018**, *333*, 519–528.

[28] Du, Y. C.; Liu, W. W.; Qiang, R.; Wang, Y.; Han, X. J.; Ma, J.; Xu, P. Shell thickness-dependent microwave absorption of core–shell Fe_3O_4@C composites. *ACS Appl. Mater. Interfaces* **2014**, *6*, 12997–3006.

[29] Zhang, Y. N.; Liu, W.; Quan, B.; Ji, G. B.; Ma, J. N.; Li, D. R.; Meng, W. Achieving the interfacial polarization on C/Fe_3C heterojunction structures for highly efficient lightweight microwave absorption. *J. Colloid Interface Sci*. **2017**, *508*, 462–468.

[30] Wang, C.; Xiong, Y.; Wang, H. W.; Jin, C. D.; Sun, Q. F. Naturally three-dimensional laminated porous carbon network structured short nano-chains bridging nanospheres for energy storage. *J. Mater. Chem. A* **2017**, *5*, 15759–15770.

[31] Fang, J. Y.; Shang, Y. S.; Chen, Z.; Wei, W.; Hu, Y.; Yue, X. G.; Jiang, Z. H. Rice husk-based hierarchically porous carbon and magnetic particles composites for highly efficient electromagnetic wave attenuation. *J. Mater. Chem. C* **2017**, *5*, 4695–4705.

[32] Lei, Y. L.; Chen, F.; Luo, Y. J.; Zhang, L. Three-dimensional magnetic graphene oxide foam/Fe_3O_4 nanocomposite as an efficient absorbent for Cr(VI) removal. *J. Mater. Sci*. **2014**, *49*, 4236–4245.

[33] Jin, H; Nishiyama, Y.; Wada, M.; Kuga, S. Nanofibrillar cellulose aerogels. *Colloids Surf. A: Phys. Eng. Aspects* **2004**, *240*, 63–67.

[34] Gan, S.; Zakaria, S.; Chia, C. H.; Chen, R. S.; Ellis, A. V.; Kaco, H. Highly porous regenerated cellulose hydrogel and aerogel prepared from hydrothermal synthesized cellulose carbamate. *PLoS One* **2017**, *12*, e0173743.

[35] Wang, X. L.; Huang, X.; Chen, Z. R.; Liao, X. P.; Liu, C.; Shi, B. Ferromagnetic hierarchical carbon nanofiber bundles derived from natural collagen fibers: Truly lightweight and high-performance microwave absorption materials. *J. Mater. Chem. C* **2015**, *3*, 10146–10153.

[36] Yu, M.; Han, Y. Y.; Li, J.; Wang, L. J. Magnetic N-doped carbon aerogel from sodium carboxymethyl cellulose/collagen composite aerogel for dye adsorption and electrochemical supercapacitor. *Int. J. Biol. Macromol*. **2018**, *115*, 185–193.

[37] Wang, Z. F.; Shen, B.; Zou, A. H.; He, N. Y. Synthesis of Pd/Fe_3O_4 nanoparticle-based catalyst for the cross-coupling of acrylic acid with iodobenzene. *Chem. Eng. J*. **2005**, *113*, 27–34.

[38] Wen, B.; Cao, M. S.; Hou, Z. L.; Song, W. L.; Zhang, L.; Lu, M. M.; Jin, H. B.; Fang, X. Y.; Wang, W. Z.; Yuan, J. Temperature dependent microwave attenuation behavior for carbon-nanotube/silica composites. *Carbon* **2013**, *65*, 124–139.

[39] Feng, J.; Pu, F. Z.; Li, Z. X.; Li, X. H.; Hu, X. Y.; Bai, J. T. Interfacial interactions and synergistic effect of CoNi nanocrystals and nitrogen-doped graphene in a composite microwave absorber. *Carbon* **2016**, *104*, 214–225.

[40] He, J. Z.; Wang, X. X.; Zhang, Y. L.; Cao, M. S. Small magnetic nanoparticles decorating reduced graphene oxides to tune the electromagnetic attenuation capacity. *J. Mater. Chem. C* **2016**, *4*, 7130–7140.

[41] Wang, L. N.; Jia, X. L.; Li, Y. F.; Yang, F.; Zhang, L. Q.; Liu, L. P.; Ren, X.; Yang, H. T. Synthesis and microwave absorption property of flexible magnetic film based on graphene oxide/carbon nanotubes and Fe_3O_4 nanoparticles. *J. Mater. Chem. A* **2014**, 2, 14940–14946.

[42] Lv, H. L.; Liang, X. H.; Ji, G. B.; Zhang, H. Q.; Du, Y. W. Porous three-dimensional flower-like Co/CoO and its excellent electromagnetic absorption properties. *ACS Appl. Mater. Interfaces* **2015**, *7*, 9776–9783.

[43] Hu, C. G.; Mou, Z. Y.; Lu, G. W.; Chen, N.; Dong, Z. L.; Hu, M. J.; Qu, L. T. 3D graphene-Fe_3O_4 nanocomposites with high-performance microwave absorption. *Phys. Chem. Chem. Phys*. **2013**, *15*, 13038–13043.

[44] Wu, Z. C.; Tian, K.; Huang, T.; Hu, W.; Xie, F. F.; Wang, J. J.; Su, M. X.; Li, L. Hierarchically porous carbons derived from biomasses with excellent microwave absorption performance. *ACS Appl. Mater. Interfaces* **2018**, *10*, 11108–11115.

[45] Cheng, Y.; Meng, W.; Li, Z. Y.; Zhao, H. Q.; Cao, J. M.; Du, Y. W.; Ji, G. B. Towards outstanding dielectric consumption derived from designing one-dimensional mesoporous MoO_2/C hybrid heteronanowires. *J. Mater. Chem. C* **2017**, *5*, 8981–8987.

[46] Meng, F. B.; Wei, W.; Chen, X. N.; Xu, X. L.; Jiang, M.; Jun, L.; Wang, Y.; Zhou, Z. W. Design of porous C@Fe_3O_4 hybrid nanotubes with excellent microwave absorption. *Phys. Chem. Chem. Phys*. **2016**, *18*, 2510–2516.

[47] Meng, F. B.; Wei, W.; Chen, J. J.; Chen, X. N.; Xu, X. L.; Jiang, M.; Wang, Y.; Lu, J.; Zhou, Z. W. Growth of Fe_3O_4 nanosheet arrays on graphene by a mussel-inspired polydopamine adhesive for remarkable enhancement in electromagnetic absorptions. *RSC Adv*. **2015**, *5*, 101121–101126.

[48] Lu, M. M.; Cao, M. S.; Chen, Y. H.; Cao, W. Q.; Liu, J.; Shi, H. L.; Zhang, D. Q.; Wang, W. Z.; Yuan, J. Multiscale assembly of grape-like ferroferric oxide and carbon nanotubes: A smart absorber prototype varying temperature to tune intensities. *ACS Appl. Mater. Interfaces* **2015**, *7*, 19408–19415.

[49] Jia, X. L.; Wang, J.; Zhu, X.; Wang, T. H.; Yang, F.; Dong, W. J.; Wang, G.; Yang, H. T.; Wei, F. Synthesis of lightweight and flexible composite aerogel of mesoporous iron oxide threaded by carbon nanotubes for microwave absorption. *J. Alloys Compd*. **2017**, *697*, 138–146.

[50] Yan, L. W.; Hong, C. Q.; Sun, B. Q.; Zhao, G. D.; Cheng, Y. H.; Dong, S.; Zhang, D. Y.; Zhang, X. H. *In situ* growth of core–sheath heterostructural SiC nanowire arrays on carbon fibers and enhanced electromagnetic wave absorption performance. *ACS Appl. Mater. Interfaces* **2017**, *9*, 6320–6331.

[51] Liu, X. F.; Hao, C. C.; Jiang, H.; Zeng, M; Yu, R. H. Hierarchical $NiCo_2O_4$/Co_3O_4/NiO porous composite: A lightweight electromagnetic wave absorber with tunable absorbing performance. *J. Mater. Chem. C* **2017**, *5*, 3770–3778.